

Enhancing the sensitivity of single microwave photon detection with bandwidth tunability.

Louis Pallegoix¹, Jaime Travesedo¹, Alexandre S. May^{1,2}, Léo Balembois¹, Denis Vion¹, Patrice Bertet^{*1} and Emmanuel Flurin^{*1}

¹*Université Paris-Saclay, CEA, CNRS, SPEC, 91191 Gif-sur-Yvette Cedex, France*

²*Alice&Bob, 53 boulevard du Général Martial Valin, 75015 Paris**

(Dated: January 14, 2025)

We report on the characteristics of a microwave photon counter device based on a superconducting transmon qubit. Its design is similar to [1], with an additional bandwidth tuning circuit that allows optimizing the device efficiency and noise. Owing to this new feature and to improvements in device fabrication, a power sensitivity of $3 \cdot 10^{-23} \text{ W}/\sqrt{\text{Hz}}$ is reached. We confirm the high performance of the device by measuring single spin microwave fluorescence.

I. INTRODUCTION

Single-photon detection has long been a fundamental tool in quantum technologies, with well-established applications in the optical domain, ranging from fluorescence microscopy [2–5] to quantum communication [6]. However, extending single-photon detection into the microwave regime presents significant challenges. The energy of microwave photons—on the order of μeV —is several orders of magnitude lower than that of optical photons, requiring detectors to operate at cryogenic temperatures to suppress thermal noise and reduce the background thermal photon population.

Despite these challenges, Single Microwave Photon Detectors (SMPDs) have emerged as critical tools for advancing quantum sensing and information processing. Their ability to detect individual microwave photons has opened new possibilities for a wide range of applications, including the detection of weak incoherent microwave emitters, such as electron spins in solids [7–9], and even searches for hypothetical dark matter particles [10, 11]. SMPDs also hold potential for primary thermometry at low temperatures [12] and for use in quantum illumination protocols [13]. Moreover, these detectors can play a key role in quantum information processing [14–16], enabling heralded entanglement between superconducting qubits [17], improving qubit readout schemes [18], and facilitating the generation of robust quantum states [19].

Various SMPD designs have been proposed and implemented, with most relying on superconducting qubits [7, 17, 20–32], quantum dots [33, 34] or bolometric detectors [35]. These devices have demonstrated promising results, achieving sensitivities in the range of 10^{-21} to $10^{-22} \text{ W}/\sqrt{\text{Hz}}$ at microwave frequencies. However, there remain limitations in terms of bandwidth, detection efficiency, and dark count rates that must be addressed to further enhance their performance.

In this work, we present an enhanced version of the SMPD introduced in Ref. [1], based on a superconducting

qubit and a four-wave mixing process. The new design integrates a frequency-tunable Purcell filter, providing control over the detection bandwidth. This tunability significantly reduces thermal noise and lowers the dark count rate down to 30 s^{-1} , improving the overall detector performance. Additionally, advancements in the fabrication process have led to an extended qubit relaxation time (T_1), which in turn enhances the detection efficiency to 0.8. As a result of these improvements, the detector achieves a power sensitivity of $3 \cdot 10^{-23} \text{ W}/\sqrt{\text{Hz}}$, representing a significant advancement over previous designs. We confirm the SMPD improved sensitivity by detecting the microwave fluorescence from a single spin.

II. SMPD PRINCIPLE OF OPERATION

A. Device design

The SMPD device (see Fig. 1a and b) consists of a transmon qubit (mode q , frequency ω_q), capacitively coupled to two harmonic oscillator modes, called respectively the buffer (mode b , frequency ω_b), and the waste (mode w , frequency ω_w). The buffer is connected to the input line of the device through another resonator at frequency ω_{pb} . The latter serves as Purcell filter to decouple the qubit from the input line, while also setting the effective buffer energy coupling rate $\kappa_{b,c}$. The total energy loss rate of the buffer resonator is $\kappa_b = \kappa_{b,c} + \kappa_{b,i}$, with $\kappa_{b,i}$ the internal losses of the buffer. The waste is connected to an output line through another Purcell filter, at frequency ω_{pw} , with a rate κ_w . Other relevant parameters are the qubit energy relaxation time T_1 and equilibrium excited state population, $p_{\text{th},q}$, which varies with the qubit temperature T as $p_{\text{th},q} = \frac{1}{e^{\frac{\hbar\omega_q}{k_B T}} - 1}$. In this formula, T is not necessarily the cryostat base temperature, as various heating effects (due to infra-red radiation in particular) may lead to a higher effective qubit temperature.

For optimal operation as an energy detector, both the frequency and bandwidth of the device need to be matched to the source of interest, be it a spin [1, 8] or a dark matter candidate [36]. Frequency tuning is achieved by inserting a

* emmanuel.flurin@cea.fr; patrice.bertet@cea.fr

SQUID in the buffer mode, resulting in a buffer frequency $\omega_b(\phi_b)$ that depends on the flux threading the buffer SQUID loop, ϕ_b . An asymmetric SQUID is purposely chosen to minimize sensitivity to flux noise. Bandwidth tuning is achieved by inserting a second SQUID in the Purcell filter mode, resulting in a buffer coupling rate $\kappa_{b,c}(\phi_{pb})$ that depends on the flux threading the Purcell SQUID loop, ϕ_{pb} . This SQUID is symmetric to maximize the bandwidth tuning range.

B. Four-Wave Mixing

The working principle of photon detection relies on a four-wave mixing (4WM) process that maps the presence or absence of a photon on the state of the transmon qubit. The non-linear element is provided by the qubit Josephson junction. The 4WM is activated by a microwave signal (called the pump, frequency ω_p) of amplitude ξ_0 , applied to the qubit via a pump line connected capacitively to the qubit (see Fig. 1). When the pump frequency approximately satisfies the relation $\omega_b + \omega_p = \omega_q + \omega_w - \chi_w$, the dominant process is described by the Hamiltonian

$$H_{4WM} = \sqrt{\chi_b \chi_w} (\xi_0 b q^\dagger w^\dagger + \xi_0^* b^\dagger q w), \quad (1)$$

where χ_b (resp. χ_w) is the qubit dispersive coupling to the buffer mode (resp. the waste mode) [20]. This Hamiltonian reversibly converts a buffer and pump photon into a qubit excitation and waste photon. Dissipation of the waste photon into the output line ensures that the process is irreversible; on the other hand, the qubit remains excited long enough to be readout subsequently, and can thus be used as a flag that frequency conversion occurred.

An approximate description is obtained by eliminating the qubit degree of freedom, yielding an effective Hamiltonian $H_{\text{eff}} = g_{4WM} b w^\dagger + h.c.$ with $g_{4WM} = \sqrt{\chi_b \chi_w} \xi_0$. It describes the parametric coupling between the buffer and waste modes, similar to the Josephson Parametric Converter for instance. Assuming that $\kappa_{b,i} \ll \kappa_{b,c}$, the efficiency for frequency conversion under this process is $\eta_{4WM} = 4C/(1+C)^2$, where $C = \frac{4\chi_b \chi_w |\xi_0|^2}{\kappa_w \kappa_b}$ is the system cooperativity. Unit efficiency is reached when $C = 1$. Physically, this occurs when the frequency conversion rate $4|g_{4WM}|^2/\kappa_w$ is equal to the input resonator coupling rate, κ_b . This condition can always be achieved by adjusting the pump frequency and amplitude (see Appendix A for more details).

C. Cyclic operation

The SMPD is operated cyclically. A cycle consists of three successive steps: Detection, Readout, and Reset (see Fig. 1c). During the detection step, which lasts T_d , the pump drive is simply switched on, with suitable amplitude

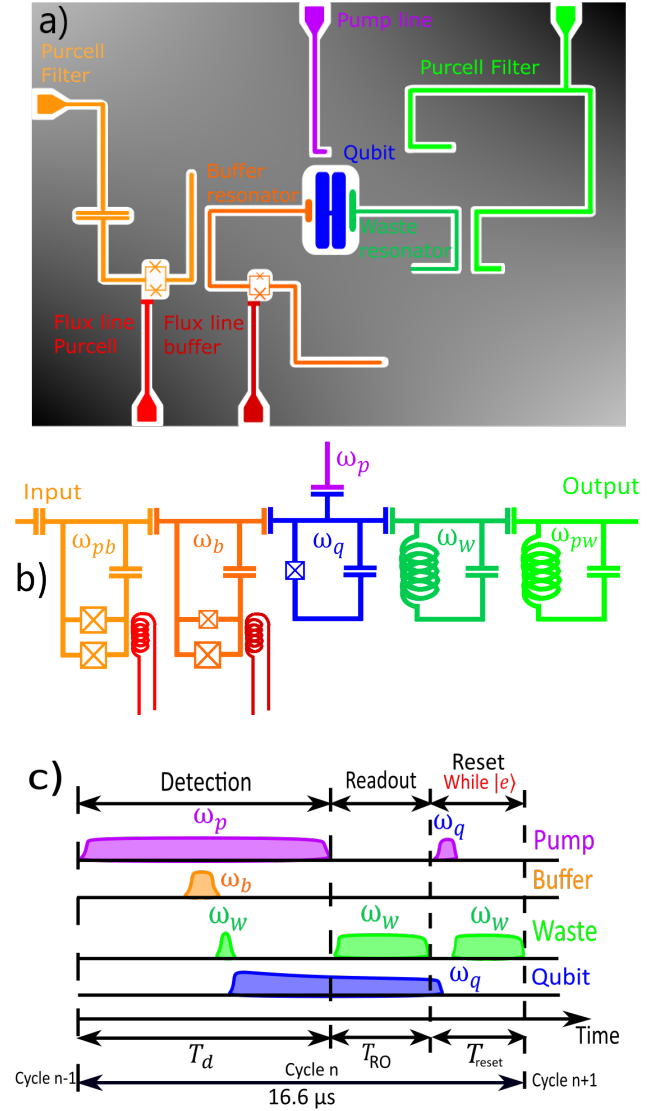


Figure 1: Overview of the device. a) Global layout of the SMPD. b) Lumped-element scheme of the SMPD. The colors of the different resonators are in accordance with their colors on the chip scheme. Note : The buffer SQUID is asymmetrical. c) Operation cycle of the SMPD. During the Detection step (duration T_d), the pump is switched on; a photon arriving in the buffer mode is converted into a photon in the waste which quickly decays, and a qubit excitation which decays in a characteristic time $T_1 \gg T_d$. Dispersive readout is performed through the waste resonator in a time T_{RO} . If the qubit is found in $|e\rangle$, a π pulse is applied, followed by qubit readout, and re-application of the reset if it is found in $|e\rangle$. This conditional reset step lasts T_{reset} . The whole cycle lasts 16.6 μ s (assuming one reset cycle).

and frequency for maximum frequency conversion. In the next step, dispersive qubit readout is achieved via the waste resonator by measuring the reflected field quadratures of a microwave tone in a time T_{RO} . We define the readout fidelity $\mathcal{F}_{\text{RO}} < 1$ as the probability to measure the qubit in the excited state after a π pulse.

In the third step, the qubit is reset in its ground state by applying a π pulse conditioned to the outcome of the previous readout being the excited state. This resets the qubit in its ground state efficiently, with a probability that can be even lower than the thermal equilibrium qubit excited state probability. In the following we will assume this reset step to be ideal. Note that the duration of the reset step T_{reset} varies from cycle to cycle due to its conditional nature. The detector duty cycle η_{cycle} is defined as the average value of $T_d/(T_d + T_{\text{RO}} + T_{\text{reset}})$.

III. FIGURES OF MERIT

In this section, we describe in somewhat detail the processes that limit the device performance as an energy detector. This performance is captured by the power sensitivity S , defined as the power that can be detected with unit signal-to-noise ratio in 1 s integration time:

$$S = \hbar\omega_b \frac{\sqrt{\alpha}}{\eta_{\text{SMPD}}}. \quad (2)$$

In this formula, η_{SMPD} is the SMPD overall detection efficiency, and α is the average number of counts per second when no signal is sent to the device. The latter can be separated in two contributions $\alpha = \alpha_{\text{err}} + \alpha_{\text{th}}$, α_{err} being the false positive events, and α_{th} the counts due the detection of thermal photons in the input line. In the following, we address each of these three quantities, with the goal of maximizing η_{SMPD} , and minimizing α_{err} and α_{th} .

A. Detection efficiency

A photon can be missed if :

- It is spectrally filtered by the detector
- The 4WM efficiency is not 1
- The qubit relaxes back in its ground state during the detection step
- Qubit excited state readout fails
- The photon hits the detector during the readout or reset steps

Therefore, the probability that a photon in the input line at frequency ω gives rise to a count is

$$\eta_{\text{SMPD}}(\omega) = \eta_{\omega} \eta_{4\text{WM}} \eta_q \mathcal{F}_{\text{RO}} \eta_{\text{cycle}}, \quad (3)$$

where the detector frequency response function is approximated by a Lorentzian of width κ_d (the detector linedwidth) such that $\eta_{\omega} = \frac{1}{1 + \left[\frac{2(\omega - \omega_b)}{\kappa_d} \right]^2}$. The qubit

efficiency $\eta_q = \frac{T_1}{T_d} (1 - e^{-\frac{T_d}{T_1}})$ can be approximated by $1 - \frac{T_d}{2T_1}$ in the limit $T_d \ll T_1$ [1]. To maximize η_{SMPD} , T_d should be optimized in order to maximize the duty cycle while keeping the cycle time well below T_1 to avoid relaxation of the qubit before readout.

B. Dark count rate

The dark count rate α_{err} is the number of counts detected per unit of time although no photon was present in the input line. It has two contributions, $\alpha_{\text{err}} = \alpha_q + \alpha_p$. First, the qubit can be found in the excited state despite the active reset procedure. This is due to the relaxation towards the thermal equilibrium value $p_{q,th}$, which takes place during the detection window with a characteristic time T_1 , giving rise to $\alpha_q = p_{q,th} (T_d/T_1) (1/(T_d + T_{\text{RO}} + T_{\text{reset}}))$ (assuming that the active reset works perfectly). The other contribution α_p is due to heating brought by the pump. Note that the readout errors causing the ground state to be erroneously detected as the excited state are negligible because we purposely choose a detection threshold that minimizes this effect.

C. Thermal counts

Thermalizing the microwave field at millikelvin temperatures is well-known to be a difficult task, because of vanishing thermal conductivity and of the large attenuation needed in the input lines. This results in an effective field temperature often significantly larger than the cryostat base temperature, and in our case in the presence of a finite flux of thermal photons at the SMPD input causing a thermal count rate of thermal origin

$$\alpha_{\text{th}} = \int_{-\infty}^{\infty} \bar{n}_{\text{th},b} \eta_{\text{SMPD}}(\omega) d\omega, \quad (4)$$

where $\bar{n}_{\text{th},b} = \frac{1}{e^{\frac{\hbar\omega_b}{k_B T}} - 1}$ the photon number per mode assuming that the field is at temperature T . Because $\kappa_d \ll \omega_b$, we get

$$\alpha_{\text{th}} = \frac{\bar{n}_{\text{th},b} \kappa_d \eta_{\text{SMPD}}(\omega_b)}{4}. \quad (5)$$

Owing to the tunable bandwidth of our device, we are here able to test the predicted proportionality between noise and detector bandwidth, as will be seen below.

Resonator	Frequency	Linewidth
Buffer Purcell	$\omega_{pb}/2\pi \in [7.26; 7.78]$ GHz	20 MHz
Buffer	$\omega_b/2\pi \in [7.70; 7.76]$ GHz	See fig. 2
Qubit	$\omega_q/2\pi = 6.533$ GHz	16 kHz
Waste	$\omega_w/2\pi = 8.475$ GHz	1.75 MHz
Waste Purcell	$\omega_{pw}/2\pi \approx 8.39$ GHz	400 MHz

Table I: Measured resonator frequencies and linewidths. The Purcell filter of the buffer and the buffer itself are tunable over the indicated interval. The buffer linewidth depends on the the Purcell frequency, as shown on fig. 2.

Resonator	Cross-Kerr to qubit
Buffer	$\chi_b/2\pi = 3.5$ MHz
Waste	$\chi_w/2\pi = 16$ MHz

Table II: Measured dispersive shifts induced by the qubit to its neighboring resonators.

IV. MEASUREMENTS

A. Device characterization

The SMPD resonators are measured with a Vector Network Analyser (VNA). Each resonance is fitted in order to determine the resonator frequency and linewidth. The result of these fits are reported in tab. I.

Figure 2a, shows $\omega_b(\phi_b)$, for several values of ϕ_{pb} . The buffer tuning range is narrow (60 MHz) and the curve is well fitted by a sinusoid [37], from which we deduce a ratio of 15 between the Josephson junction critical currents of the asymmetric SQUID. Little cross-talk between the ϕ_b and ϕ_{pb} is observed, as evidenced by the weak dependence of $\omega_b/2\pi$ on ϕ_{pb} .

From the fits of the buffer resonance curves, we extract $\kappa_{b,i} = 2.2 \cdot 10^5 \text{s}^{-1}$, and $\kappa_{b,c}$, the internal loss and coupling rates, respectively. $\kappa_{b,c}/2\pi$, is shown in Fig. 2c as a function of the detuning from the Purcell, $\omega_b - \omega_{pb}$. A large tuning range is observed, ranging from ~ 10 kHz up to ~ 3 MHz. The tuning curve is identical for all values of buffer resonator frequency (see Fig. 2c). The buffer is over-coupled in a large parameter range (corresponding to $\kappa_{b,c} \gg \kappa_{b,i}$), which is desirable for SMPD operation, as buffer internal losses further reduce η_{4WM} [1].

Qubit readout is performed at the waste resonator frequency when the qubit is in the excited state, $\omega_W - \chi_W$, to minimize the chances to excite it out of the ground state and cause unwanted dark counts, with a readout duration $T_{RO} = 0.8 \mu\text{s}$. Readout histograms are shown in Fig. 3a, yielding the readout fidelity $\mathcal{F}_{RO} = 0.87$ and equilibrium excited state population $p_{th,q} = 8.5 \cdot 10^{-4}$. The qubit lifetime is $T_1 = 70 \mu\text{s}$ (see Fig. 3b), and the coherence time measured under a Ramsey sequence is $T_2^* = 20 \mu\text{s}$. The dispersive shifts χ_b and χ_w are reported in Table II. Active reset is performed as explained in Section IIC [1].

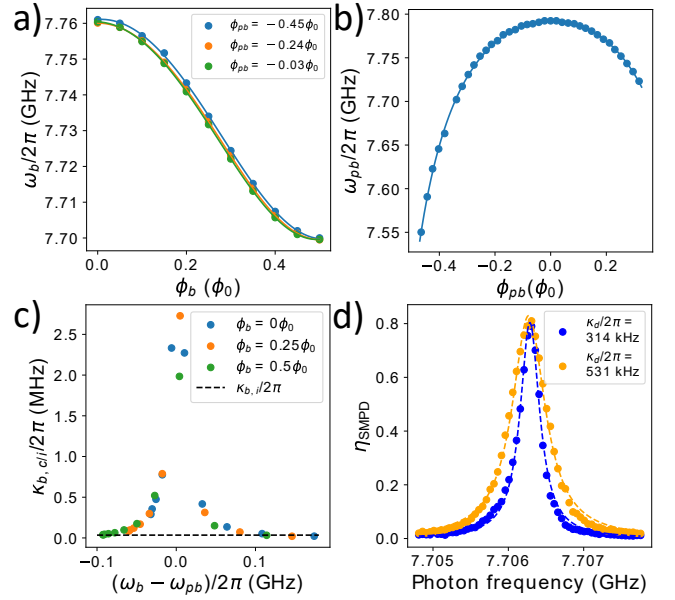


Figure 2: Tunability curves. a) Full blue circles are the measured frequency of the Purcell filter, ω_{pb} , as a function of the flux bias sent to its SQUID Φ_{pb} . Solid line is a fit assuming a symmetric SQUID. b) Solid circles are the measured frequency of the buffer resonator, ω_b , as a function of the flux bias applied to its SQUID, Φ_b , for several values of Φ_{pb} (blue is $-0.45\Phi_0$, orange is $-0.24\Phi_0$, green is $-0.03\Phi_0$). The solid lines are sinusoidal fits, yielding the asymmetry between the buffer SQUID junctions. c) Full circles show the measured coupling rate of the buffer resonator to the 50Ω line, as a function of its detuning from the Purcell filter, $\omega_b - \omega_{pb}$, for 3 different values of Φ_b : blue for $\Phi_b = 0$, orange for $\Phi_b = 0.25\Phi_0$, green for $\Phi_b = 0.5\Phi_0$. The dashed line shows the buffer internal losses, $\kappa_{b,i}$. d) Full circles are measured SMPD efficiency, η_{SMPD} , as a function of signal frequency ω , for $\kappa_b/2\pi = 170$ kHz (blue) and 280 kHz (orange). Dashed lines are Lorentzian fits yielding the SMPD bandwidth $\kappa_d/2\pi$, equal to respectively 314 kHz and 531 kHz.

B. Four-Wave-Mixing tuning

The Four-Wave mixing condition is found by sending a pump tone at frequency ω_p together with a signal at frequency ω into the SMPD input, followed by qubit readout. Sweeping ω_p and ω , the 4WM condition is identified by an enhanced qubit excited state when the signal is present, which vanishes when it is switched off (see Fig. 4). The pump power is then tuned to reach unit cooperativity (see Appendix and Fig. 4).

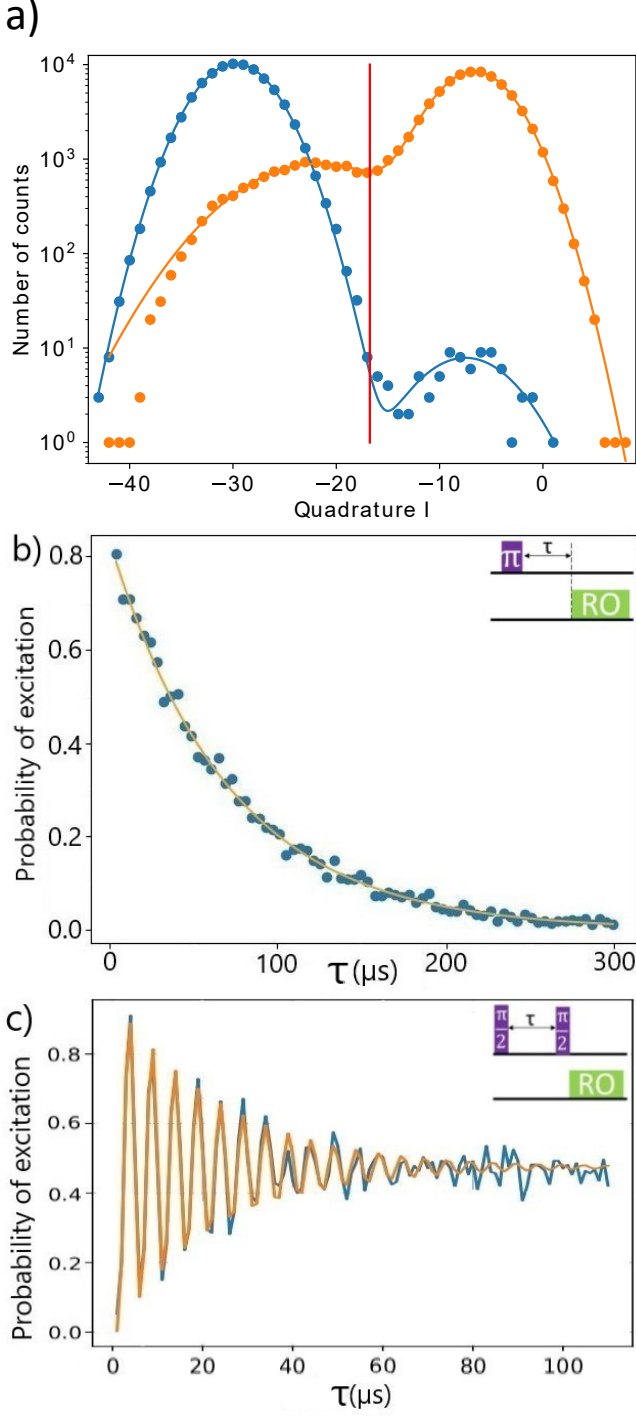


Figure 3: a) Qubit readout histograms after 95650 sequences, in absence of any preparation pulse (blue full circles), and after a π pulse (orange full circles). Solid lines are fits by a sum of two Gaussians centered on the two quadrature I values corresponding to the ground and excited states, yielding $p_{q,th} = 8.5 \cdot 10^{-4}$, and $\mathcal{F}_{RO} = 0.87$. The red line shows the threshold. b) Qubit excited state probability following a π pulse, yielding $T_1 = 70 \mu\text{s}$. c) Qubit Ramsey fringes yielding $T_2^* = 20 \mu\text{s}$. Insets : corresponding pulse sequences. Purple pulses are sent through the drive line, green through the readout (RO) line.

C. Cyclic operation : Detector Bandwidth and Dark counts

We now turn to the SMPD operation in cyclic mode. The detection step duration is set to $T_d = 15 \mu\text{s}$. When no photon is sent to the device, the qubit is most often in the ground state at the end of the sequence, implying that no reset is needed, and that the average cycle duration is very close to $T_d + T_{RO} = 15.8 \mu\text{s}$, yielding the duty cycle $\eta_{\text{cycle}} = 0.95$. From Eq. 3, we expect η_{SMPD} to reach 0.74.

The experimental η_{SMPD} is measured by counting the number of clicks detected over 1 second integration time, at the same time that a calibrated signal is sent to the SMPD input. The signal power is calibrated using the qubit as a detector (see [1] and Appendix B). The result is plotted as a function of input frequency ω in Fig. 2d. The maximum efficiency reaches $\eta_{\text{SMPD}} = 0.8$. This is even slightly higher than the predicted value, which implies in particular that the Four-Wave-Mixing efficiency $\eta_{4\text{WM}}$ is very close to 1. Fitting $\eta_{\text{SMPD}}(\omega)$ by a Lorentzian, we obtain the detector bandwidth κ_d . Two curves are shown, obtained for two different values of κ_b . The maximum efficiency is unchanged, but the detector bandwidth is changed according to κ_b . This confirms that the SMPD bandwidth can be adjusted by tuning κ_b via the Purcell filter frequency. We measure $\kappa_d/2\pi = 315 \text{ kHz}$ for $\kappa_b/2\pi = 170 \text{ kHz}$, and $\kappa_d/2\pi = 530 \text{ kHz}$ for $\kappa_b/2\pi = 280 \text{ kHz}$, thus confirming the approximate relation $\kappa_d \simeq 2\kappa_b$ (see Appendix A).

Dark counts are measured by recording photon counting traces in the absence of any input signal (see Table III, where the detector bandwidth was $\kappa_d/2\pi = 170 \text{ kHz}$). To obtain the various contributions to the dark counts, the traces are systematically measured with pump off (yielding α_q), pump on detuned by 20 MHz (yielding $\alpha_q + \alpha_p = \alpha_{\text{err}}$), and pump on tuned to the 4WM conditions (yielding $\alpha = \alpha_{\text{err}} + \alpha_{\text{th}}$). At 10 mK, we obtain $\alpha_q = 8 \text{ s}^{-1}$, $\alpha_p = 2 \text{ s}^{-1}$, and $\alpha_{\text{th}} = 21 \text{ s}^{-1}$. Combined with the measured efficiency, we obtain a power sensitivity $S = 3 \cdot 10^{-23} \text{ W}/\sqrt{\text{Hz}}$, a factor of three better than the previous state-of-the-art [1], which corresponds to an order of magnitude gain in measurement time.

Time traces are similarly measured by varying the cryostat temperature T . The values of α_q and α_{th} are shown as a function of T in Fig. 5. The qubit contribution increases with temperature, because of the higher excited state probability at equilibrium; it is well fitted by $\alpha_{q,0} + K_q p_{\text{th},q}(T)$, with $\alpha_{q,0} = 7 \text{ s}^{-1}$ and $K_q = 2.2 \cdot 10^4 \text{ s}^{-1}$. The value of K_q is slightly larger than the predicted $(T_d/T_1)(1/(T_d + T_{RO} + T_{\text{reset}}))$ (see Section IIIB), which is $1.4 \cdot 10^4 \text{ s}^{-1}$, possibly because of a reduction of T_1 at higher temperature. The thermal contribution also increases with temperature; it is well fitted by $\alpha_{\text{th},0} + K_{\text{th}} \bar{n}_{\text{th},b}$, with $\alpha_{\text{th},0} = 31 \text{ s}^{-1}$, and $K_{\text{th}} = 2 \cdot 10^5 \text{ s}^{-1}$. This value is in quantitative agreement with the expected $\eta_{\text{SMPD}} \kappa_d/4 = 2.1 \cdot 10^5 \text{ s}^{-1}$, thus providing an independent confirmation of the efficiency estimate reported earlier.

The equilibrium qubit excitation (without active reset)

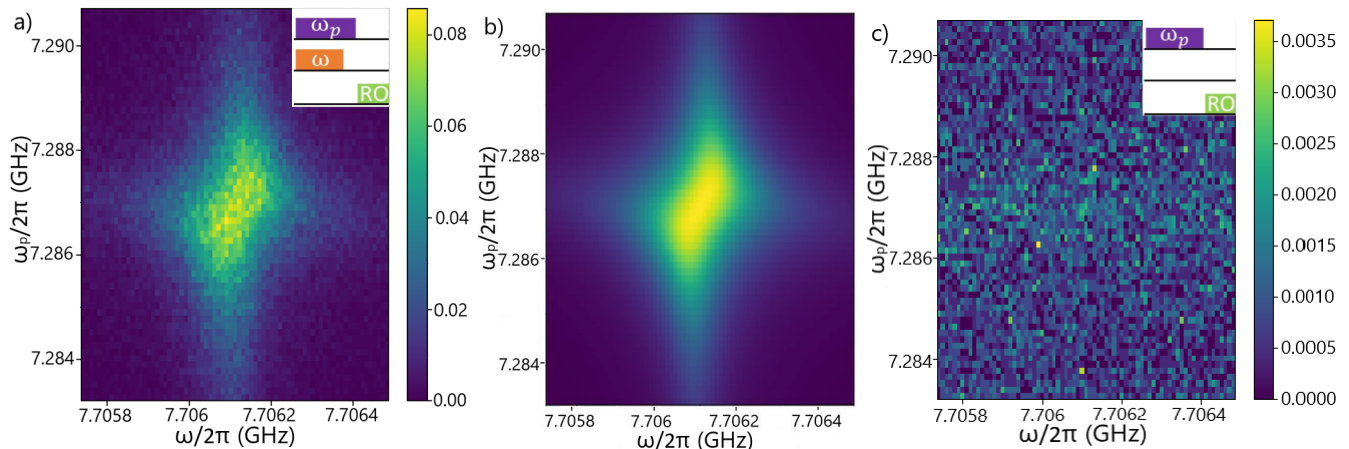


Figure 4: a) Four-wave mixing pattern : this color plot shows the measured qubit excited state as a function of pump frequency ω_p and signal frequency ω . b) Fit from a two-coupled cavity model. To fit the data, the value of the cooperativity C is adjusted. Here, the value is $C = 0.99$ (see Appendix A). Other fit parameters are the buffer linewidth, $\kappa_b/2\pi = 120$ kHz and waste linewidth, $\kappa_w/2\pi = 1.75$ MHz. c) Same experiment as a with the signal tone switched off. The qubit is excited only when the signal is close to ω_b , and the pump verifies the 4-Wave Mixing condition. Insets : corresponding pulse sequences. Purple pulses are sent through the pump/drive line, orange pulses through the signal/input line and green pulses through the waste/readout (RO) line. Pumping, signal and readout pulses are respectively 15 μ s, 10.5 μ s and 800 ns long.

$p_{th,q}$ at 10 mK translates into an effective qubit temperature of 42 mK. The thermal photon rate $\alpha_{th,0}$ measured at 10 mK translates into a mean photon number per mode of $1.5 \cdot 10^{-4}$ and thus to an effective temperature of 40 mK. This is higher than the mean photon number expected from our line attenuation, which we estimate to be below $\sim 2 \cdot 10^{-5}$. Our results therefore confirm the well-known difficulty to thermalize microwave fields and modes to temperatures much lower than ~ 40 mK, possibly due to the difficulty of perfectly thermalizing microwave components. It is interesting to note that SMPD devices are ideally well suited to study this phenomenon, which represents a major issue for superconducting quantum computers.

D. Dependence on detection bandwidth

We finally study the SMPD figures of merit as a function of detection bandwidth, at the lowest temperature of 10 mK. We measure the maximum value of $\eta_{SMPD}(\omega)$ and α as a function of κ_d (see Fig. 6). We observe that η_{SMPD} increases with κ_d , although the dependence is very weak as soon as the SMPD bandwidth is above 250 kHz. This is expected since the measurements are performed with a monochromatic tone. The reduction in efficiency at the lowest value of κ_d may be attributed to the contribution of internal buffer losses, as well as possible transient effects that effectively shorten the detection time T_d .

The false positive rate α on the other hand scales linearly with κ_d , as expected from Eq. 5. The fitted slope is $1.6 \cdot 10^{-5}$, in agreement with the expected $\eta \bar{n}_{th,b}/4$ yielding a thermal mode occupation $\bar{n}_{th,b} = 0.8 \cdot 10^{-4}$,

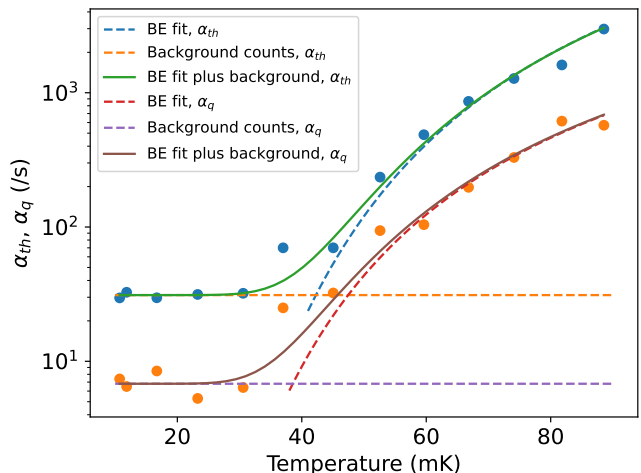


Figure 5: Measured α_{th} (blue full circles) and α_q (orange full circles) as a function of the cryostat's temperature T , for a detection bandwidth $\kappa_d/2\pi = 170$ kHz. The solid green line is a fit of α_{th} to $\alpha_{th,0} + K_{th}\bar{n}_{th,b}(T)$, yielding $\alpha_{th,0} = 31s^{-1}$ and $K_{th} = 2 \cdot 10^5s^{-1}$. The solid brown line is a fit of α_q to $\alpha_{q,0} + K_q p_{th,q}(T)$, yielding $\alpha_{q,0} = 7s^{-1}$ and $K_q = 2.2 \cdot 10^4s^{-1}$. The dashed lines are the separated Bose-Einstein and constant components of the respective fits.

slightly lower than in the measurements of Fig. 5 and corresponding to a mode temperature of 38 mK. The intercept at $\kappa_d = 0$ is $11.6s^{-1}$, consistent with the error rate α_{err} measured with pump detuned. Overall, the observed linear dependence of α_{th} on κ_d proves that these



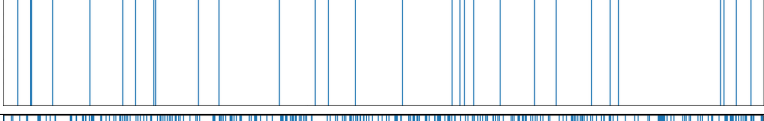



Temperature	Pump state	$\kappa_d/2\pi$	One-second click sequence	Click rate
10 mK	Off	Not relevant		8/s
10 mK	Detuned	Not relevant		10/s
10 mK	Tuned	170 kHz		31/s
50 mK	Tuned	170 kHz		344/s
60 mK	Tuned	170 kHz		621/s
90 mK	Tuned	170 kHz		3614/s

Table III: Photon counting traces taken in different conditions. First line : Mixing chamber temperature is 10 mK and the pump is off, yielding α_q . Second line : Mixing chamber temperature is 10 mK and pump is switched on, but 20 MHz detuned from the four-wave mixing condition. This yields $\alpha_{\text{err}} = \alpha_q + \alpha_p$. Third line : Mixing chamber temperature is 10 mK and the pump is on at the 4WM condition, yielding $\alpha_{\text{err}} + \alpha_{\text{th}}$. Three following lines : Mixing chamber temperature is risen and the count rate rises accordingly, as detailed on fig. 5.

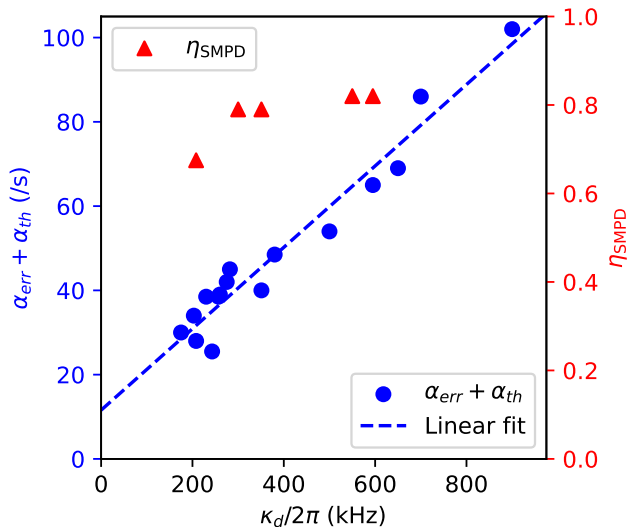


Figure 6: Blue full circles are the measured total dark counts, $\alpha_{\text{err}} + \alpha_{\text{th}}$, as a function of SMPD bandwidth κ_d . Dashed line is a linear fit, with slope $1.5 \cdot 10^{-5}$, and intercept 11.6s^{-1} . Red triangles show the measured efficiency at resonance, η_{SMPD} .

counts are indeed due to thermal photons impinging on the SMPD input line. Not much can be inferred about their spectrum, apart from the fact that it appears to be flat on the scale of the detection bandwidth (~ 1 MHz).

E. Single-spin measurements

We confirm the high efficiency of the detector by measuring the microwave fluorescence from a single electronic spin. The setup closely follows refs [8] and [38], and is schematically depicted in Fig. 7. The electronic spin is an Er^{3+} ion in a CaWO_4 matrix and is coupled to a superconducting resonator to enhance its radiative decay rate Γ_R . The spin is excited by a π pulse with near unit probability. It then relaxes radiatively by emitting a photon, which is either absorbed by the spin resonator internal losses, or emitted in the line, after which it may reach the SMPD detector or be absorbed by the losses in-between the two devices. The SMPD buffer ω_b is tuned to the spin and resonator frequency. The spin-to-click probability is therefore $\eta = \eta_{\text{reso}}\eta_{\text{loss}}\eta_{\text{SMPD}}(\omega_b)$, with $\eta_{\text{reso}} = 0.6$ in this device (described in more detail elsewhere [38]).

The spin microwave fluorescence curve is shown in

Fig. 7. It is well fitted by an exponential decay with time constant $\Gamma_R^{-1} = 1.24$ ms on top of a constant background, due to the SMPD dark counts. From the integral below the fluorescence curve, we obtain $\eta = 0.4$. This implies that the microwave power absorption in-between the spin device and the SMPD is $\eta_{loss} = 0.85$, a very plausible value given that the line includes a superconducting cable, a circulator, and an infra-red filter. This provides an independent confirmation of the high efficiency reached by this SMPD device and of its interest for single-spin spectroscopy.

V. CONCLUSION

We have demonstrated a microwave photon counter with tunable frequency (in the 7 GHz range) and bandwidth (between ~ 100 kHz and ~ 1 MHz). The device has a maximum efficiency of 0.8, and its noise can be reduced by lowering the bandwidth. At an input bandwidth of 200 kHz, we demonstrate a record power sensitivity of $3 \cdot 10^{-23} \text{ W}/\sqrt{\text{Hz}}$. The device is well suited to detect emitters with a narrow line, and will find applications in single-spin magnetic resonance [38, 39] as well as haloscope-based dark matter search [36].

ACKNOWLEDGEMENTS

We acknowledge technical support from P. Sénat, D. Duet, P.-F. Orfila and S. Delprat, and are grateful for fruitful discussions within the Quantronics group. We acknowledge support from the Agence Nationale de la Recherche (ANR) through the MIRESPIN (ANR-19-CE47-0011) project. We acknowledge support of the Région Ile-de-France through the DIM QUANTIP, from the AIDAS virtual joint laboratory, and from the France 2030 plan under the ANR-22-PETQ-0003 grant. This project has received funding from the European Union Horizon 2020 research and innovation program under the project OpenSuperQ100+, and from the European Research Council under the grant no. 101042315 (INGENIOUS). We acknowledge IARPA and Lincoln Labs for providing the Josephson Traveling-Wave Parametric Amplifier.

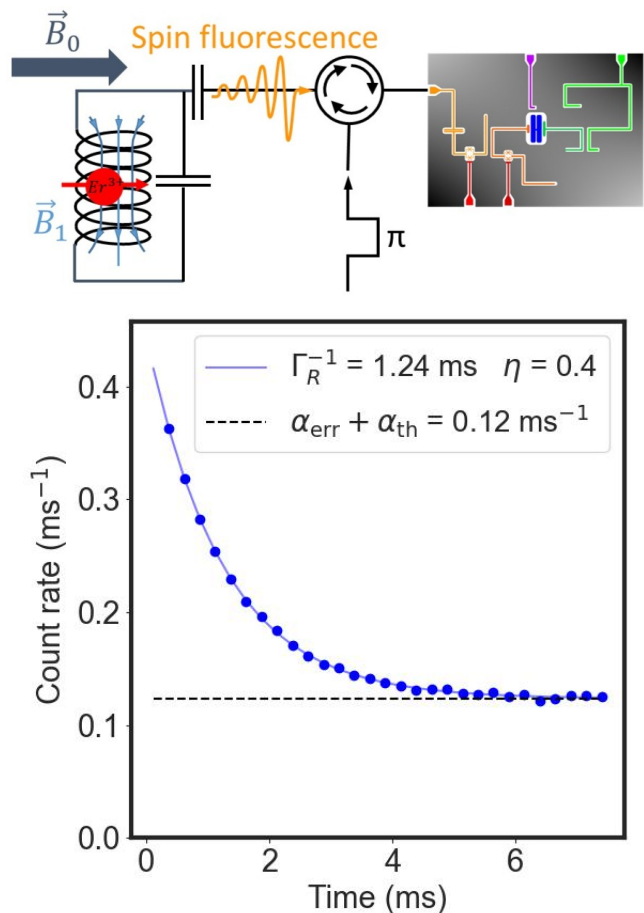


Figure 7: Microwave fluorescence of an individual Er^{3+} electron spin in a CaWO_4 host crystal matrix at 10 mK, detected by the SMPD reported here operated with $\kappa_d/2\pi = 500$ kHz. Top : scheme of the experiment. The Er^{3+} spin is magnetically coupled to the microwave field \vec{B}_1 of an LC resonator and Zeeman tuned to resonance by a field $\|\vec{B}_0\| = 460$ mT. The spin is excited by a π pulse, and the photon it emits upon radiative relaxation is detected by the SMPD. Graph : blue full circles are the measured count rate following a π pulse excitation of the spin, as a function of the time. Solid blue line is an exponential fit, from which we extract the spin lifetime $\Gamma_R^{-1} = 1.24$ ms and spin-to-click efficiency, $\eta = 0.4$. Note that the noise floor is slightly higher than expected from Fig. 6, possibly due to a different wiring scheme in the cryostat.

APPENDIX A : PUMP CALIBRATION

In this section we detail the pump parameters tuning procedure. The optimal pump frequency should satisfy the 4WM condition, $\omega_{4WM} = \omega_q + \omega_w - \chi_w - \omega_b$.

The pump amplitude is chosen by recording two-dimensional plots such as shown in Fig. 4 of the main text, where the qubit excited state probability is recorded as a function of pump and signal frequency, ω_p and ω , respectively, for various pump powers. Each plot is then fitted to the following formula [40] :

$$|S_{w \leftarrow b}(\delta, \delta_p)|^2 = \frac{4C}{\left| 1 + C - 4 \frac{\delta(\delta + \delta_p)}{\kappa_b \kappa_w} + 2i \frac{\delta}{\kappa_b} + 2i \frac{\delta + \delta_p}{\kappa_w} \right|^2} \quad (6)$$

with $\delta = \omega - \omega_b$ is the signal-buffer detuning, and $\delta_p = \omega_p - \omega_{4WM}$ the pump detuning from the 4WM condition.

If all detunings are zero, eq. 6 becomes :

$$|S_{w \leftarrow b}(\delta = 0, \delta_p = 0)|^2 = \frac{4C}{(1 + C)^2} \quad (7)$$

The maximum of eq. 7 is reached for $C = 1$ and its value is 1.

The fit returns the value of C , and after a few iterations the condition $C = 1$ is readily achieved.

Note that the full width at half maximum along the signal frequency axis of $|S_{w \leftarrow b}(\delta, \delta_p)|^2$ is the detection bandwidth of the SMPD:

$$\kappa_d = \sqrt{2} \sqrt{\sqrt{\kappa_b^2 \kappa_w^2 + \left(\frac{\kappa_b - \kappa_w}{2}\right)^4} - \left(\frac{\kappa_b - \kappa_w}{2}\right)^2} \quad (8)$$

When $\kappa_b \ll \kappa_w$ (as is the case in this work), the formula can be approximated as

$$\kappa_d \approx 2\kappa_b \quad (9)$$

APPENDIX B : EFFICIENCY MEASUREMENT

Measuring the SMPD efficiency starts by estimating the power at the buffer input. This is achieved by using the qubit as a detector. Ramsey fringes are shifted by Δ_q and dephased by Γ_q according to the equation:

$$\Delta_q + i\Gamma_q = \frac{-4\chi_b |\epsilon|^2}{(\kappa_b + i\chi_b)^2 + 4\delta^2}, \quad (10)$$

with ϵ the complex amplitude of the intra-cavity field. The efficiency is then simply computed by dividing the number of clicks per second by the number of photons per second at the device input.

APPENDIX C : SMPD FABRICATION

We now describe the fabrication recipe of the SMPD presented in this paper.

C1 : Substrate preparation

The process starts from a two-inch, double-side polished sapphire wafer. This wafer is dipped in a piranha solution made of 2/3 of sulfuric acid and 1/3 of hydrogen peroxyde (in volume) during 20 minutes. Then, it is rinsed with water and dried by dinitrogen blow. After that, the wafer is loaded into an RF reactive sputterer together with a tantalum target. The targeted thickness of tantalum sputtering is between 80 and 90 nm. The sputtering process shall be performed while the wafer is heated up to 600°C in order to get alpha phase tantalum.

The wafer is then prepared for dicing. In that regard, UV III is spincoated over the wafer during 60 seconds at 3000 rpm with an acceleration of 2000 rpm/s. This is followed by a postbake at 120°C during 3 minutes.

C2 : Circuit etching

After dicing, the protective UV III layer is removed by shooting IPA with a pissette on the chosen chip during 15 seconds, then again during 5 seconds. For further cleaning, the chip is dipped during 5 minutes in a bath of acetone with strong ultrasounds, then in another bath of isopropanol (IPA) during 3 minutes, still with strong ultrasounds. In the following, it is dried by dinitrogen blow and dipped in a piranha solution during 20 minutes. The chip is then rinsed with water, dehydrated with IPA, dried by dinitrogen blow and further dehydrated on a hotplate at 120°C during 5 minutes. Then comes the spincoating of AZ1518 during 60 seconds at 3000 rpm with an acceleration of 2000 rpm/s. The postbake is performed on hotplate during 2 minutes at 115°C. The circuit is then patterned using a UV LASER direct writer. A supplementary exposure is needed at the edge bead. The development is performed in pure MF319 during 60 seconds and stopped with water. The chip is dried by dinitrogen blow and hardbaked on hotplate during 2 minutes at 115°C. Eventually, the circuit is etched by dipping in Transene 111 (1/3 nitric acid, 1/3 hydrofluoric acid and 1/3 water) during 20 seconds sharp. There is no need for agitation during etching. Rinsing is performed by a first bath of water during 20 seconds with agitation, then in a second bath of water for transport between benches.

C3 : Chip cleaning and oxide removal

After the etching step, the chip shall be re-cleaned before moving forward to the e-beam related steps. Recently, we have added an oxide removal step in the process

which has not been applied to the sample presented here. First of all, the sample is dipped in a bath of acetone during 5 minutes for removing AZ1518, then in another bath of IPA during 3 minutes, then finally in piranha solution during 2 minutes. The chip is rinsed with water, dehydrated with IPA and dried by dinitrogen blow.

In the recently added oxidation step, the chip is dipped during 20 minutes in buffered oxide etchant (BOE), rinsed with a first bath of water during 20 seconds with agitation, then in a second bath of water for transport between benches, dehydrated with IPA, dried by dinitrogen blow and dehydrated further on hotplate during 5 minutes at 120°C.

C4 : Preparation of e-beam bilayer

A first layer made of MAA EL-6 is spincoated during 60 seconds at 4000 rpm with an acceleration of 1000 rpm/s. Postbake is performed on hotplate during 5 minutes at 172°C. Then comes the spincoating of a second layer made of PMMA 950k A6 during 60 seconds at 3000 rpm with an acceleration of 2000 rpm/s. Postbake, on a hotplate at 175°C, lasts 15 minutes.

The substrate being made of sapphire, there is no way the electrons escape through the substrate during lithography. Therefore, the bilayer shall be metallised for preventing charge effects. In that regard, a layer of 7 nm of aluminum is evaporated over the bilayer at a rate of 0.2 nm/s. There is no need for a good vacuum for this evaporation step, a pressure of about 10^{-6} hPa is enough.

C5 : E-beam lithography

Given the need of the simultaneous presence of Josephson junctions of very different sizes over the device, the Manhattan process has been chosen. Due to the absence of a 100 kV EBL in our laboratory, we have developed an adapted version of this process using a bilayer with a reversed aspect ratio (a layer of MAA about 170 nm thick under a layer of PMMA about 580 nm thick). With our Raith e-LINE system, we are using the following parameters :

- Magnification : $\times 1000$
- Base dose : $250\mu C/cm^2$
- Relative dose factor : 1.5 for "big" junctions' main pattern (about 1 μm edge size), 1.7 for "small" junctions' main pattern (about 200 nm edge size or less), 0.3 for undercut boxes.
- Voltage : 25 kV
- Aperture : 10 μm
- Current : About 20 pA
- Writefield : $100 \times 100\mu m^2$

C6 : Aluminum etching and resist development and descum

Before developing the e-beam resist, one shall remove the metallisation layer. Aluminum etching is performed by dipping the chip in a solution of potassium hydroxyde (KOH) of 10 g/L in water during 30 seconds. It is then rinsed by dipping 3 seconds in water, then 3 seconds in IPA. The development itself begins right after : The chip is dipped during 45 seconds in a solution made of 1/4 methylisobutylketone (MIBK) and 3/4 IPA (in volume). Development is stopped by dipping in IPA during 15 seconds. The chip and the bilayer are dried by nitrogen blow first, then on a hotplate at 70°C during 1 minute. The resist mask is finally cleaned in a dioxygen plasma asher during 10 seconds, with a pressure of 0.2 hPa and an ionising power of 75 W.

C7 : Josephson junctions evaporation

For evaporating Josephson junction, a good vacuum is required (at least below $5 \cdot 10^{-7}$ hPa). Given that we are using the Manhattan process, the evaporator shall be featured with a planetary rotation. The parameters informed here work for one of our Plassys MEB 550S system.

First of all, the surface is prepared by argon milling with an incidence angle of 0°. The ion gun is tuned with filament submitted to 500 V and 25 mA, and acceleration grid to 100 V. Shutter is off ion beam trajectory 2 times 5 seconds, with 1 minute of rest between each. Then comes the evaporation of the first layer of aluminum. It is performed with an angle of 30° and at a rate of 1 nm/s. A thickness of 29 nm is asked to the evaporator in order to obtain an actual thickness of 25 nm. This first layer is oxidised by a mixture of dioxygen and argon at 10 hPa during 5 minutes. The sample holder is rotated around the planetary axis of 90° in order to evaporate along the orthogonal direction of the Manhattan pattern. Finally, the second evaporation of aluminum is performed with the same parameters (30° angle and 1 nm/s rate) except that a thickness of 69 nm is asked for in order to get an actual thickness of 60 nm.

C8 : Final lift off

The lift off is performed in two successive baths of acetone at 60°C. Blowing with a Pasteur pipette helps for removal. The sample is then brought back to room temperature with a non-heated bath of acetone. It is then dehydrated in IPA and finally dried by dinitrogen blow.

- [1] L. Balembois, J. Travesedo, L. Pallegoix, A. May, E. Billaud, M. Villiers, D. Estève, D. Vion, P. Bertet, and E. Flurin, Cyclically operated microwave single-photon counter with sensitivity of 10^{-22} W/ $\sqrt{\text{Hz}}$, *Phys. Rev. Appl.* **21**, 014043 (2024).
- [2] M. Orrit and J. Bernard, Single pentacene molecules detected by fluorescence excitation in a p-terphenyl crystal, *Physical Review Letters* **65**, 2716 (1990), publisher: American Physical Society.
- [3] T. A. Klar, S. Jakobs, M. Dyba, A. Egner, and S. W. Hell, Fluorescence microscopy with diffraction resolution barrier broken by stimulated emission, *Proceedings of the National Academy of Sciences of the United States of America* **97**, 8206 (2000).
- [4] E. Betzig, G. H. Patterson, R. Sougrat, O. W. Lindwasser, S. Olenych, J. S. Bonifacino, M. W. Davidson, J. Lippincott-Schwartz, and H. F. Hess, Imaging intracellular fluorescent proteins at nanometer resolution, *Science (New York, N.Y.)* **313**, 1642 (2006).
- [5] C. Bruschini, H. Homulle, I. M. Antolovic, S. Burri, and E. Charbon, Single-photon avalanche diode imagers in biophotonics: review and outlook, *Light, Science & Applications* **8**, 87 (2019).
- [6] N. Gisin, G. Ribordy, W. Tittel, and H. Zbinden, Quantum cryptography, *Review of Modern Physics* **74**, <https://doi.org/10.1103/RevModPhys.74.145> (2002), publisher : American Physical Society.
- [7] E. Albertinale, L. Balembois, E. Billaud, V. Ranjan, D. Flanigan, T. Schenkel, D. Estève, D. Vion, P. Bertet, and E. Flurin, Detecting spins by their fluorescence with a microwave photon counter, *Nature* **600**, 434 (2021), publisher: Nature Publishing Group.
- [8] Z. Wang, L. Balembois, M. Rančić, E. Billaud, M. Le Dantec, A. Ferrier, P. Goldner, S. Bertaina, T. Chanelière, D. Esteve, D. Vion, P. Bertet, and E. Flurin, Single-electron spin resonance detection by microwave photon counting, *Nature* **619**, 276 (2023), number: 7969 Publisher: Nature Publishing Group.
- [9] E. Billaud, L. Balembois, M. L. Dantec, M. Rančić, E. Albertinale, S. Bertaina, T. Chanelière, P. Goldner, D. Estève, D. Vion, P. Bertet, and E. Flurin, Microwave fluorescence detection of spin echoes, *Physical Review Letters* <https://doi.org/10.1103/PhysRevLett.131.100804> (2023).
- [10] S. K. Lamoreaux, K. A. van Bibber, K. W. Lehnert, and G. Carosi, Analysis of single-photon and linear amplifier detectors for microwave cavity dark matter axion searches, *Physical Review D* **88**, 035020 (2013), publisher: American Physical Society.
- [11] A. V. Dixit, S. Chakram, K. He, A. Agrawal, R. K. Naik, D. I. Schuster, and A. Chou, Searching for Dark Matter with a Superconducting Qubit, *Physical Review Letters* **126**, 141302 (2021), publisher: American Physical Society.
- [12] M. Scigliuzzo, A. Bengtsson, J.-C. Besse, A. Wallraff, P. Delsing, and S. Gasparinetti, Primary Thermometry of Propagating Microwaves in the Quantum Regime, *Physical Review X* **10**, 041054 (2020), publisher: American Physical Society.
- [13] R. Assouly, R. Dassonneville, T. Peronnin, A. Bienfait, and B. Huard, Quantum advantage in microwave quantum radar, *Nature Physics* **19**, 1418 (2023), publisher: Nature Publishing Group.
- [14] R. Raussendorf, D. E. Browne, and H. J. Briegel, Measurement-based quantum computation on cluster states, *Physical Review A* **68**, 022312 (2003), publisher: American Physical Society.
- [15] H. J. Briegel, D. E. Browne, W. Dür, R. Raussendorf, and M. Van den Nest, Measurement-based quantum computation, *Nature Physics* **5**, 19 (2009), publisher: Nature Publishing Group.
- [16] S. Bartolucci, P. Birchall, H. Bombin, H. Cable, C. Dawson, M. Gimeno-Segovia, E. Johnston, K. Kieling, N. Nickerson, M. Pant, F. Pastawski, T. Rudolph, and C. Sparrow, *Fusion-based quantum computation* (2021).
- [17] A. Narla, S. Shankar, M. Hatridge, Z. Leghtas, K. Sliwa, E. Zalys-Geller, S. Mundhada, W. Pfaff, L. Frunzio, R. Schoelkopf, and M. Devoret, Robust Concurrent Remote Entanglement Between Two Superconducting Qubits, *Physical Review X* **6**, 031036 (2016), publisher: American Physical Society.
- [18] A. Opremcak, I. V. Pechenezhskiy, C. Howington, B. G. Christensen, M. A. Beck, E. Leonard, J. Suttle, C. Wilen, K. N. Nesterov, G. J. Ribeill, T. Thorbeck, F. Schlenker, M. G. Vavilov, B. L. T. Plourde, and R. McDermott, Measurement of a superconducting qubit with a microwave photon counter, *Science* **361**, 1239 (2018).
- [19] J.-C. Besse, S. Gasparinetti, M. C. Collodo, T. Walter, A. Remm, J. Krause, C. Eichler, and A. Wallraff, Parity detection of propagating microwave fields, *Physical Review X* (2020).
- [20] R. Lescanne, S. Deléglise, E. Albertinale, U. Réglade, T. Capelle, E. Ivanov, T. Jacqmin, Z. Leghtas, and E. Flurin, Irreversible Qubit-Photon Coupling for the Detection of Itinerant Microwave Photons, *Physical Review X* **10**, 021038 (2020).
- [21] G. Romero, J. J. García-Ripoll, and E. Solano, Microwave Photon Detector in Circuit QED, *Physical Review Letters* **102**, 173602 (2009), publisher: American Physical Society.
- [22] F. Helmer, M. Mariani, E. Solano, and F. Marquardt, Quantum nondemolition photon detection in circuit QED and the quantum Zeno effect, *Physical Review A* **79**, 052115 (2009), publisher: American Physical Society.
- [23] S. R. Sathyamoorthy, L. Tornberg, A. F. Kockum, B. Q. Baragiola, J. Combes, C. Wilson, T. M. Stace, and G. Johansson, Quantum Nondemolition Detection of a Propagating Microwave Photon, *Physical Review Letters* **112**, 093601 (2014), publisher: American Physical Society.
- [24] O. Kyriienko and A. S. Sørensen, Continuous-Wave Single-Photon Transistor Based on a Superconducting Circuit, *Physical Review Letters* **117**, 140503 (2016), publisher: American Physical Society.
- [25] S. R. Sathyamoorthy, T. M. Stace, and G. Johansson, Detecting itinerant single microwave photons, *Comptes Rendus. Physique* **17**, 756 (2016).
- [26] X. Gu, A. F. Kockum, A. Miranowicz, Y.-x. Liu, and F. Nori, Microwave photonics with superconducting quantum circuits, *Physics Reports Microwave photonics with superconducting quantum circuits*, **718-719**, 1 (2017).
- [27] B. Royer, A. L. Grimsmo, A. Choquette-Poitevin, and A. Blais, Itinerant Microwave Photon Detector, *Physical Review Letters* **120**, 203602 (2018), publisher: American Physical Society.

- [28] Y.-F. Chen, D. Hover, S. Sendelbach, L. Maurer, S. T. Merkel, E. J. Pritchett, F. K. Wilhelm, and R. McDermott, Microwave photon counter based on Josephson junctions, *Physical Review Letters* [10.1103/PhysRevLett.107.217401](https://doi.org/10.1103/PhysRevLett.107.217401) (2011).
- [29] K. Koshino, K. Inomata, T. Yamamoto, and Y. Nakamura, Implementation of an impedance-matched λ system by dressed-state engineering, *Physical Review Letter* [10.1103/PhysRevLett.111.153601](https://doi.org/10.1103/PhysRevLett.111.153601) (2013).
- [30] K. Inomata, Z. Lin, K. Koshino, W. D. Oliver, J.-S. Tsai, T. Yamamoto, and Y. Nakamura, Single microwave-photon detector using an artificial Λ -type three-level system, *Nature Communications* **7**, 12303 (2016), arXiv:1601.05513 [cond-mat, physics:quant-ph].
- [31] J.-C. Besse, S. Gasparinetti, M. C. Collodo, T. Walter, P. Kurpiers, M. Pechal, C. Eichler, and A. Wallraff, Single-Shot Quantum Nondemolition Detection of Individual Itinerant Microwave Photons, *Physical Review X* **8**, 021003 (2018), publisher: American Physical Society.
- [32] S. Kono, K. Koshino, Y. Tabuchi, A. Noguchi, and Y. Nakamura, Quantum non-demolition detection of an itinerant microwave photon, *Nature Physics* **14**, 546 (2018), arXiv:1711.05479 [quant-ph].
- [33] C. H. Wong and M. G. Vavilov, Quantum efficiency of a single microwave photon detector based on a semiconductor double quantum dot, *Physical Review A* [10.1103/PhysRevA.95.012325](https://doi.org/10.1103/PhysRevA.95.012325) (2017).
- [34] A. Ghirri, S. Cornia, and M. Affronte, Microwave photon detectors based on semiconducting double quantum dots, *Sensors* <https://doi.org/10.3390/s20144010> (2020).
- [35] G.-H. Lee, D. K. Efetov, W. Jung, L. Ranzani, E. D. Walsh, T. A. Ohki, T. Taniguchi, K. Watanabe, P. Kim, D. Englund, and K. C. Fong, Graphene-based Josephson junction microwave bolometer, *Nature* **586**, 42 (2020), number: 7827 Publisher: Nature Publishing Group.
- [36] C. Braggio, L. Balembis, R. Di Vora, Z. Wang, J. Travesedo, L. Pallegoix, G. Carugno, A. Ortolan, G. Ruoso, U. Gambardella, D. D'Agostino, P. Bertet, and E. Flurin, [Quantum-enhanced sensing of axion dark matter with a transmon-based single microwave photon counter](https://arxiv.org/abs/2403.02321) (2024), arXiv:2403.02321 [hep-ex, physics:quant-ph].
- [37] A. Blais, A. L. Grimsmo, S. Girvin, and A. Wallraff, Circuit quantum electrodynamics, *Reviews of Modern Physics* (2021).
- [38] J. Travesedo, J. O'Sullivan, L. Pallegoix, Z. W. Huang, P. Hogan, P. Goldner, T. Chaneliere, S. Bertaina, D. Esteve, P. Abgrall, D. Vion, E. Flurin, and P. Bertet, [All-microwave readout, spectroscopy, and dynamic polarization of individual nuclear spins in a crystal](https://arxiv.org/abs/2408.14282) (2024), arXiv:2408.14282 [cond-mat, physics:quant-ph].
- [39] J. O'Sullivan, J. Travesedo, L. Pallegoix, Z. Huang, P. Hogan, P. Goldner, D. Esteve, D. Vion, P. Bertet, and E. Flurin, Individual solid-state nuclear spin qubits with coherence exceeding seconds (2024), coming soon.
- [40] E. Albertinale, *Measuring spin fluorescence with a microwave photon detector*, Ph.D. thesis, Université Paris-Saclay (2021).